# Observational study of formation mechanism, vertical structure and dust emission of dust devils over the Taklimakan Desert, China

**Article** *in* Journal of Geophysical Research Atmospheres · March 2016

Impact Factor: 3.43 · DOI: 10.1002/2015JD024256



**9 authors**, including:

Tianliang Zhao

Nanjing University of Information Science & …

**64** PUBLICATIONS **1,141** CITATIONS

SEE PROFILE

Feng Liu

University of Illinois, Urbana-Champaign

**7** PUBLICATIONS **11** CITATIONS

SEE PROFILE

Yongxiang Han

**14** PUBLICATIONS **205** CITATIONS

SEE PROFILE

Wangki Yuen

University of Illinois, Urbana-Champaign

**10** PUBLICATIONS **38** CITATIONS

SEE PROFILE

AGU PUBLICATIONS

JGR

Journal of Geophysical Research: Atmospheres

RESEARCH ARTICLE
10.1002/2015JD024256

**Key Points:**
- The critical conditions in atmospheric boundary layer for dust devil formation over the desert
- Dust particles in central updrafts and peripheral downdrafts were asymmetrically distributed
- The vertical flux of near-surface dust emissions in a TD's dust devil was estimated

**Correspondence to:**
T. Zhao,
tlzhao@nuist.edu.cn

**Citation:**
Liu, C., T. Zhao, X. Yang, F. Liu, Y. Han, Z. Luan, Q. He, M. Rood, and W. Yuen (2016), Observational study of formation mechanism, vertical structure, and dust emission of dust devils over the Taklimakan Desert, China, *J. Geophys. Res. Atmos.*, *121*, doi:10.1002/2015JD024256.

Received 25 SEP 2015
Accepted 12 MAR 2016
Accepted article online 19 MAR 2016



# Observational study of formation mechanism, vertical structure, and dust emission of dust devils over the Taklimakan Desert, China

**Chong Liu[1], Tianliang Zhao[1], Xinghua Yang[2], Feng Liu[1], Yongxiang Han[1], Zhaopeng Luan[1], Qing He[2], Mark Rood[3], and Wangki Yuen[3]**

[1]Collaborative Innovation Center on Forecast and Evaluation of Meteorological Disasters, Key Laboratory for Aerosol-Cloud-Precipitation of China Meteorological Administration, Nanjing University of Information Science and Technology, Nanjing, China, [2]Institute of Desert Meteorology, China Meteorological Administration, Urumqi, China, [3]Department of Civil and Environmental Engineering, University of Illinois at Urbana-Champaign, Urbana, Illinois, USA

**Abstract** A field observation of dust devils was conducted at Xiaotang over the Taklimakan Desert (TD), China, from 7 to 14 July 2014. The measurements of dust devil opacity with the digital optical method and the observed atmospheric boundary layer conditions were applied to investigate the dust devils' formation mechanism, vertical structure, and dust emissions. The critical conditions in the atmospheric boundary layer for dust devil formation were revealed with the land-air surface temperature difference of higher than 15°C, the enhanced momentum flux and sensible heat flux up to 0.54 kg m$^{-1}$ s$^{-2}$ and 327 W m$^{-2}$, respectively, the weak vertical wind shear with the low wind shear index $\alpha < 0.10$, and the unstable stratification in the lower atmosphere. Based on observed dust opacities, it is identified that a typical dust devil was vertically structured with central updrafts and peripheral downdrafts of dust particles with the asymmetrically horizontal distribution of dust in a rotating dust column. The vertical flux of near-surface dust emissions was also estimated in a range from $5.4 \times 10^{-5}$ to $9.6 \times 10^{-5}$ kg m$^{-2}$ s$^{-1}$ for a typical dust devil event over TD.

## 1. Introduction

As common phenomena in the atmosphere, dust devils are vertical vortices with dust particle-loaded strong convection, driven by uneven surface heating and rising of near-surface air because of insolation [*Balme and Greeley*, 2006]. The dust devils are most active over the hot and flat surfaces [*Mattsson et al.*, 1993], in height from a few meters to over 1 km and in diameter of less than 100 m with different shapes due to different terrains and atmospheric boundary layers [*Metzger et al.*, 1999]. Dust devils, whatever the size or shape, do major harm to air quality in arid and semiarid areas [*Gillette and Sinclair*, 1990; *Mattsson et al.*, 1993]. The passage of dust devils across the surface can carry particulate matter, leave tracks, and increase aerosol concentrations, which influences the planetary albedo and its radiation balance [*Malin and Edgett*, 2001; *Reiss et al.*, 2010, 2011] potentially playing an important role in maintaining and replenishing the background dust aerosols in the atmosphere and reducing visibility [*Whelley and Greeley*, 2008].

Owing to the importance of dust devils in the atmosphere and climate change, dust devils have been studied by field observations, experimental analyses, and numerical simulations. *Ives* [1947] and *Sinclair* [1964] observed the general characteristics of dust devils including dust devil diameters, inside and outside temperature and pressure differences, and rotational speed and radial velocities. Dust devils' high-rotating speed ($15 \pm 2$ m s$^{-1}$) was observed a few meters above the ground [*Gu et al.*, 2003; *Rennó et al.*, 1998]. *Sinclair* [1973] found that dust devils' diameters were usually tens of meters, and dust column height was lower than 600 m in Arizona. *Hess et al.* [1988] in Australia observed dust devils with diameters of 32–141 m with a dust column height of 300–660 m. *Carroll and Ryan* [1970] noticed that dust devils were on a shorter timescale of 5–15 min. Only rare occurrences of large dust devils had lifetimes from 30 min to several hours [*Metzger*, 1999; *Mattsson et al.*, 1993]. *Oke et al.* [2007] reported that dust devils tended to form when environmental wind speeds ranged from 1.5 to 7.5 m s$^{-1}$. In a field experiment of the ground heat flux and dust sediment flux in the Arizona desert, *Renno et al.* [2004] estimated the vertical surface dust emissions of $1.0 \times 10^{-4}$ kg m$^{-2}$ s$^{-1}$ for a dust plume and $1.0 \times 10^{-3}$ kg m$^{-2}$ s$^{-1}$ for a dust devil. With the infrared images, *Lorenz and Myers* [2005] discovered that particles within dust devils were strongly

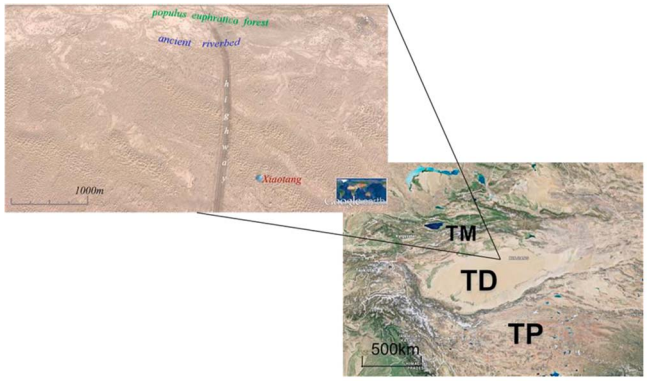


**Figure 1.** The location of observation site, Xiaotang, in the northern edge of TD (from the Google Earth). The TM and TP stand for the Tianshan Mountains and the Tibetan Plateau, respectively, in the right lower panel.

heated by insolation by the warm Earth's surface and the atmosphere near the Earth's surface. Digital cameras were utilized to study dust devils by *Lorenz et al.* [2010]; they proved that the cameras can be used for systematic surveys and in principle can have a lower opacity threshold than a fatigued human observer might. Although there were many field observations for macroscopic description of dust devils, few involved reporting of environmental and boundary conditions of dust devils, especially in the Taklimakan Desert (TD), which is located in the Tarim Basin of Northwest China with an area of 337,000 km$^2$, as the second largest shifting sand desert in the world, with about 85% made up of shifting sand dunes.

Field observations of dust devils in TD reported here were conducted from 7 to 14 July 2014, by applying the digital optical method (DOM) [*Du et al.*, 2007, 2013] and equipment to measure atmospheric boundary layer conditions. It is noteworthy that DOM is a novel and efficient way to measure the particle plumes at a distance of 100 m ± 50 m and was used to derive the opacity of dust devils from captured images during this field experiment. Based on the dust aerosol opacities calculated with DOM, the vertical structures and dust emissions were estimated during dust devil episodes. This study contributes to the structural characteristics of dust devils and consequently the dust emission parameterizations that can be used in numerical models to better understand the impact of dust devils on environment and climate through altering the dust distribution and radiation budget.

## 2. Observation Methods

### 2.1. Meteorological Observation

The observation site, Xiaotang (40.8°N, 84.3°E; Figure 1), is located over the northern edge of TD with the annual mean precipitation of less than 40 mm. The surface sand samples in this region are dominated by fine diameter sand (0.125–0.25 mm) and very fine diameter sand (0.0625–0.125 mm) with 48.35% and 30.05% in total samples, respectively [*Zhang et al.*, 2008]. A gradient detection system was installed on a 10 m tower to observe wind speed; temperature; humidity at heights of 0.5, 1, 2, 4, and 10 m; and wind directions at heights of 2 m and 10 m with the anemoscope (model WAA151). The air temperature was measured at heights of 2 m by the 10 m (model HMP45D) with the gradient observation system. Ground temperature was measured by an infrared thermometer (model SI-111), which is a precision infrared radiometer that was installed at 50 cm height above the ground to determine the surface temperature without physical contact. A flux detection instrument (model CSAT3/Li-cor7500) was installed 3 m above the ground to measure the wind speed and temperature fluctuations in zonal, meridional, and vertical directions. Table 1 lists the basic meteorological elements measured from 7 to 14 July 2014.

### 2.2. DOM Observation

The transmission model of DOM [*Du*, 2007] quantifies the dust devil opacity in contrast to a uniform sky background, e.g., clear and overcast sky based on the radiance from the dust devil and its atmospheric background (Figure 2). In Figure 2, $N_0$ is the radiance from the uniform sky and $N_b$ is the equivalent radiance value recorded by the camera in terms of pixel values passing through the dust-free atmosphere. If the extinction of the background atmosphere around the dust devil is negligible compared to that of the dust devil with making sure that the sun is to be oriented to the back of the camera, $N_b = N_0$. Then the dust devil's opacity ($\tau$) is determined by DOM [*Du et al.*, 2007] as follows

$$\text{Opacity } (\tau) = \frac{1 - \frac{N_p}{N_b}}{1 - K}. \quad (1)$$

The proportionality coefficient $K$ with value range of 0.16–0.21 is controlled by weather conditions and optical properties of aerosol particles [*Kim et al.*, 2007]. $N_p$ is the radiance value caused by radiance from

**Table 1.** Basic Meteorological Elements of 7–14 July 2014 in Xiaotang

| Date | Temperature (°C) | | Relative Humidity (%) | | Wind | | Precipitation (mm) | Duration of Sunshine (h) |
|---|---|---|---|---|---|---|---|---|
| | Mean | 14:00 | Mean | 14:00 | Speed (m/s) | Direction | | |
| 7 July | 25.2 | 29.6 | 30 | 24 | 3.3 | SE | 0 | 1.1 |
| 8 July | 22.1 | 29.1 | 45 | 30 | 4.2 | SSE | 0 | 7.2 |
| 9 July | 20.8 | 24 | 67 | 54 | 2.8 | North | 8.7 | 12.2 |
| 10 July | 24.3 | 29.9 | 49 | 25 | 4.6 | SW | 0 | 12.6 |
| 11 July | 27.2 | 32.8 | 35 | 20 | 3.9 | NW | 0 | 12.4 |
| 12 July | 29.4 | 35.7 | 34 | 16 | 1.8 | North | 0 | 12.4 |
| 13 July | 31.1 | 37.6 | 30 | 12 | 2.8 | NW | 0 | 12.4 |
| 14 July | 32.9 | 38.7 | 23 | 15 | 3.6 | North | 0 | 9.9 |

the dust devil and path radiance of the atmosphere. Images analyzed by DOM were obtained with a digital still camera (SONY DSC-P100) to convert the received light energy into discrete digital signals, referred to as pixel value (PV). By using the DOM transmission model, the dust devil's opacity is calculated from the pixel information of the photographs based on the radiance ratios ($N_p/N_b$) in formula (1). The camera calibration values depend on the camera used for the tests and were determined during laboratory testing at the University of Illinois at Urbana-Champaign seeing that camera vendors do not provide such information. The calibration constants are (a, b, and c) for the camera used during the field campaign. The resultant polynomial that was used to analyze the images is

$$\ln(E) = a\ln^2(\mathrm{PV}) + b\ \ln(\mathrm{PV}) + c, \tag{2}$$

where $E$ is the amount of exposure, PV is pixel value, and a, b, and c are calibration constants, with the values of 0.41, −2.11, and 2.61, respectively.

Since the exposure $E$ is proportional to the radiance, the radiance ratio can be calculated by using $\mathrm{PV}_p$ as the PV for the dust devil and $\mathrm{PV}_b$ as the PV of the atmospheric background without the dust devil with the following equation:

$$\frac{N_p}{N_b} = \frac{E_p}{E_b} = \frac{\exp\left(f\left(\mathrm{PV}_p\right)\right)}{\exp\left(f\left(\mathrm{PV}_b\right)\right)} \tag{3}$$

Gray-scale averaging was used for all images. Autoexposure was used with the camera to determine the exposure time and the *f*-number. White balance was not used during the field campaigns. Although the gamma or standard Red Green Blue (sRGB) response functions are not considered with DOM, DOM does relate exposure to PV as a nonlinear function. Thus, the nonlinear response is taken into account in DOM.

We manually took pictures when we saw a dust devil, relying on the human eye to distinguish the dust devils. Therefore, there was no minimum size of dust devil or opacity value, besides what a human detects. The dust devils' height and diameter were estimated by measuring the physical length of bushes on the ground as the reference. The effective spatial resolution was advised to observe dust devils at a distance of 100 m ± 50 m so that we could more accurately estimate the diameter and height of dust devils.

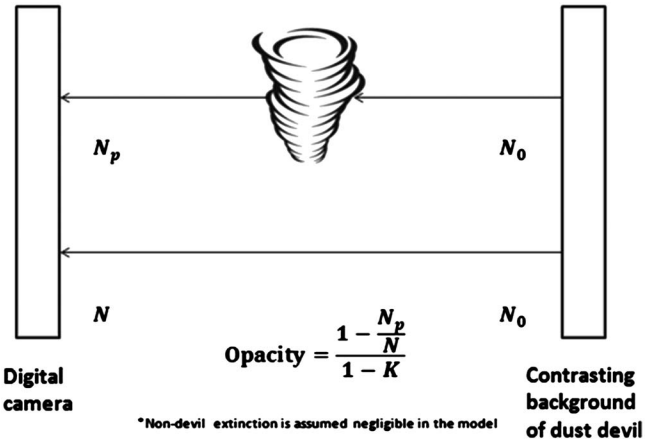


**Figure 2.** A schematic diagram of the transmission model DOM for calculating dust aerosol opacity of dust devils.

## 3. Results and Discussion

### 3.1. Surface Heating

Heating in the near-surface air by insolation could be represented with temperature differences between land and near-surface air. The hourly

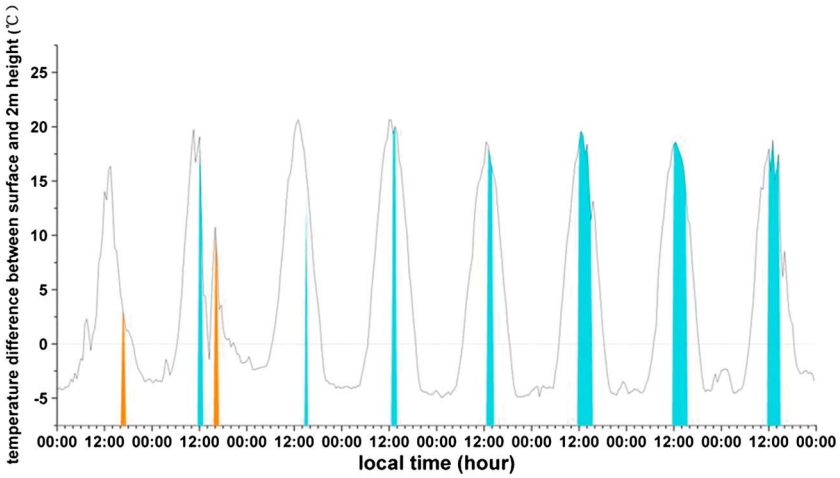


**Figure 3.** Hourly changes of temperature differences between surface and air at 2 m (black curves) during 7–14 July 2014. Blue and yellow bars represent the periods of dust devils and dust storm events, respectively.

variations in the land-air temperature differences are shown in Figure 3. As previously mentioned, the air temperature was measured at a height of 2 m, and the ground temperature was measured by the infrared thermometer. Blue and yellow regions represent the lasting periods of dust devils and dust storm events, respectively. Driven by the diurnal change of insolation, the land-air temperature differences varied diurnally between 16.4–24.0°C at noon (local time, same for hereinafter) and −3.5 to −5.1°C at midnight, reflecting a strong diurnal cycle of the sensible heat flux over the desert surface of TD. In arid and semiarid areas with less evaporation, sensible heat flux dominates the land-air energy exchange. The strong surface heating could be an important cause in the dust devil formation [*Hallett and Hoffer*, 1971; *Metzger*, 1999; *Snow and McClelland*, 1990]. Radiation on the Earth's surface increases with the sunrise reaching a peak at noon, enhancing the sensible heat flux from land to air. Surface heating could increase air temperature and decrease air density in the near-surface layers. Hot and light air mass rises to form the thermal convection, driven by thermal buoyancy in the convection boundary layer. According to the field observation as shown in Figure 3, the land-air surface temperature difference exceeding 15°C could be a critical condition to form dust devils over TD.

Large land-air temperature differences with weak dust devils were also observed on 9 July 2014, when rainfall happened in the morning. The surface moisturized by rainfall at the observation site greatly restrained the dust devil occurrence. The formation of a dust devil could be affected not only by convective heating of buoyancy but also by frictional dissipation [*Lyons et al.*, 2008].

### 3.2. Atmospheric Boundary Layer Conditions

As previously mentioned, we measured the wind speed and air temperature fluctuations in the near-surface layers by the flux detection instrument CSAT3/Li-cor7500. We used eddy covariance to obtain the momentum flux and the sensible heat flux of the environment within 100 m ± 50 m from dust devils [*Mamtimin et al.*, 2008]. Figure 4 shows the momentum flux, the friction velocity, and the sensible heat flux during 12 and 13 July 2014. Momentum flux (in the unit of $kg\,m^{-1}\,s^{-2}$) is the rate of momentum transfer over a unit area. The positive and negative momentum fluxes represent the upward and downward directions. In turbulent flow, the momentum flux is caused by inertial forces in the fluid due to the action of eddies (i.e., Reynolds stresses). Sensible heat flux represents the magnitude of heat energy transfer between the Earth's surface and the atmosphere by conduction and convection, as an important component of Earth's surface energy budget [*Roland*, 2000].

As shown in Figure 4, the momentum flux, the friction velocity, and the sensible heat flux fluctuated significantly, reflecting the vigorous variations in diurnal cycles of the boundary layer. Enough momentum flux can bring more dust from the desert's surface to the atmosphere. Dust devils exhibited strong momentum flux in the near-surface atmosphere, changed with the daily averages between 0.09 and 0.13 $kg\,m^{-1}\,s^{-2}$ during 2 days, and then achieved 0.54 $kg\,m^{-1}\,s^{-2}$ at 15:40 P.M. on 13 July (Figure 4). The patterns of change in the

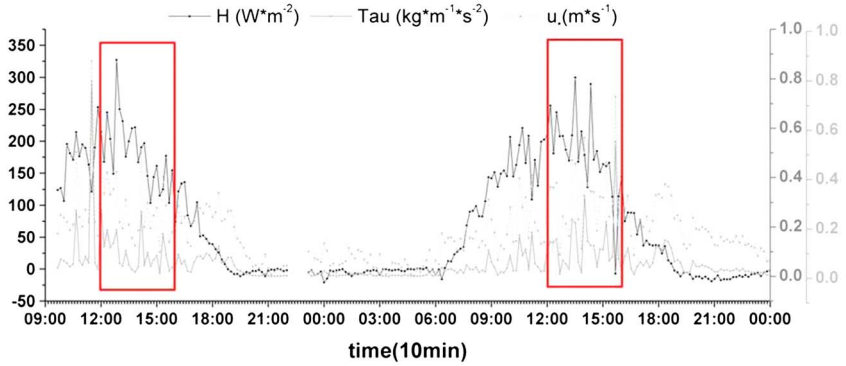


**Figure 4.** The 10 min averaged changes in the momentum flux (gray line), the friction velocity (gray dash line), and the sensible heat flux (black line) during 12 and 13 July 2014. Red boxes indicate when the dust devils were observed.

friction velocity and momentum flux were similar with a high correlation coefficient 0.91 (Figure 4). At the same time, the sensible heat flux increased up to 327 W m$^{-2}$ with daily averages of 178–181 W m$^{-2}$ (Figure 4), indicating the huge heat losses from the ground for heating the lower lying air layers to give rise to an unstable stratification.

In the boundary layer, the wind speed changes significantly with height, building a strong vertical wind shear, caused by dynamic and thermodynamic factors. The dynamic factor is associated with the surface friction effects, namely, the roughness of the ground; the thermodynamic factor is mostly connected with atmospheric vertical stability. The atmospheric stability varies with temperature and weather conditions, changing the wind shear property accordingly [*Han et al.*, 2008]. The wind shear index $\alpha$ is defined with the changes of wind speed between 2 m and 10 m in the atmosphere with the following formula [*Farrugia*, 2003]

$$\alpha = \frac{\ln(S2/S1)}{\ln(H2/H1)}, \tag{4}$$

where S1 and S2 are the wind speeds in the unit of m s$^{-1}$ at the heights of H1 and H2, in the unit of meters. The values of wind shear index $\alpha$ represent the magnitudes of vertical wind shear. Figure 5 exhibits the hourly change of $\alpha$ over the observation period. High (low) wind shear at midnight (noon) generally coincided with low (high) solar radiation (Figure 5). From 10:00 to 15:00, wind shear dropped to low levels, when strong solar radiation resulted in the high instability and the well vertical mixing in the boundary layer (Figure 5). From 20:00 to 6:00 of the next day, the values of $\alpha$ were high for the strong wind shear. *Rennó et al.* [1998] found that the intensity of a dust devil depends on the depth of the convective plume and the existence of low vertical wind shears. Low vertical shears may produce disturbances of surface air and provide initial rotary movement.

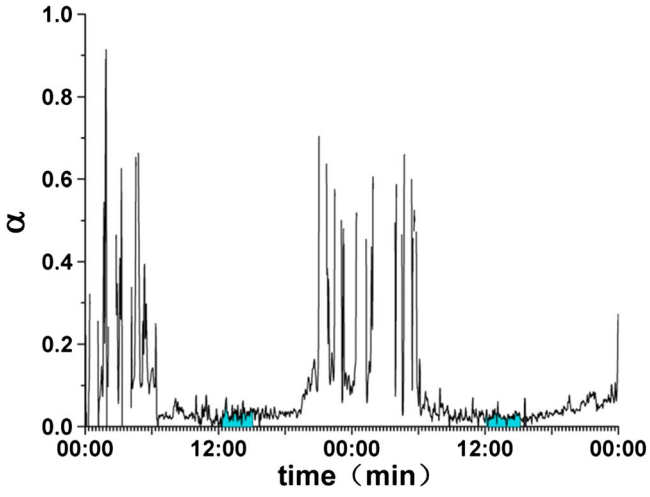


**Figure 5.** Minutely changes in the wind shear index from 12 to 13 July 2014. Blue shaded intervals are the periods of dust devils.

Based on the conditions of the ground-air temperature difference, the wind shear, the momentum flux, and the sensible heat flux, Figure 6 shows a histogram of the relevant values, for times when dust devils were seen and when they were not. The frequency of ground-air temperature difference from 18°C to 20°C during the observation periods was 0.05, while it could be up to 0.34 during the dust devils. The mean and standard deviation of the ground-air temperature difference were −3.1°C and 8.4°C, respectively, during the observation periods, while

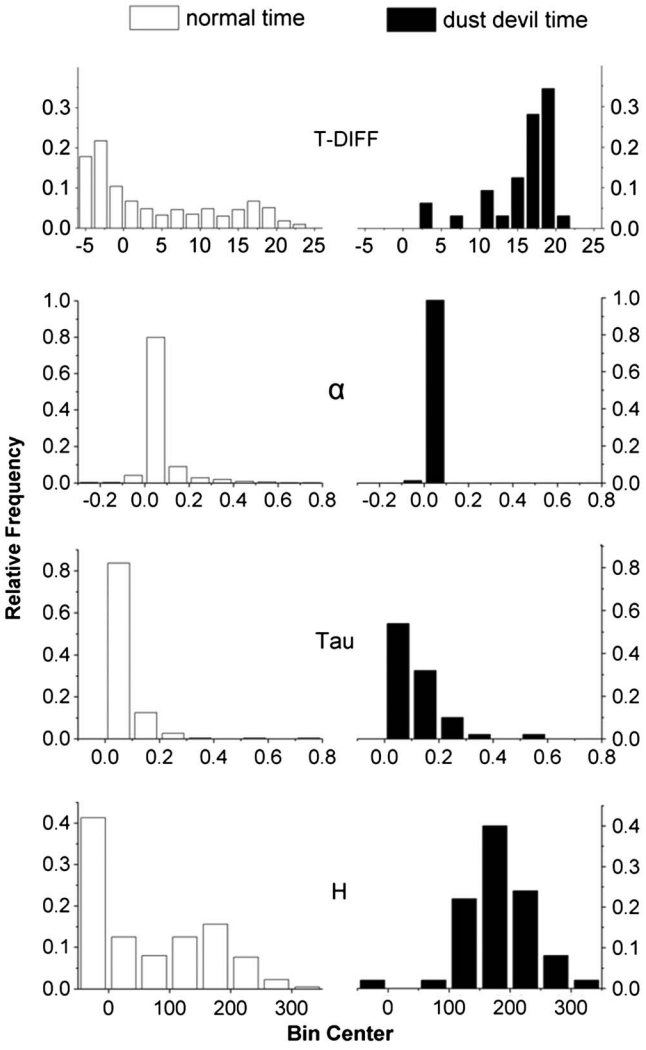


**Figure 6.** A histogram of the ground-air temperature difference ($T-$ diff, °C), the wind shear ($\alpha$), the momentum flux (Tau, kg m$^{-1}$ s$^{-2}$), and the sensible heat flux (H, W m$^{-2}$), for times when dust devils were seen (black shaded) and when they were not seen (unshaded), from 12 to 13 July 2014.

they were 15.7°C and 4.4°C, respectively, during dust devil observations. When dust devils were observed, the frequency of the wind shear $\alpha$ was between 0 and 0.1 during 98% of these events. Based on our study, the weak vertical wind shear with the wind shear index $\alpha < 0.10$ could be identified as the boundary layer conditions maintaining the dust devils. A scatterplot of air-ground temperature difference and wind shear is shown in Figure 7. The trend lines with and without dust devil observations are very similar, reflecting the similar relationship between wind shear and surface heating represented by air-ground temperature difference. Obviously, dust devils occurred when the air-ground temperature difference was greater than 11°C and the wind shear was lower than 0.05. The large values ($\geq$0.1 kg m$^{-1}$ s$^{-2}$) of the momentum flux (Tau) occurred at a higher proportion when dust devils were observed, which increased from 0.17 to 0.46 during those observations. The highest frequency reached 40% of the sensible heat flux (H) from 150 to 200 W m$^{-2}$ during dust devil observations, while the frequency from 150 to 200 W m$^{-2}$ was only 15% during the whole day.

Considering the contemporary boundary layer paradigms and concepts, Figure 8 presents the Monin-Obukhov length $L$ (m) and the dimensionless stability factor $(z-d)/L$ ($z$ is the height of the stable surface layer and $d$ is the zero-plane displacement). When $L$ and $(z-d)/L$ are negative, the atmosphere is unstable to encourage dust devil occurrences. The values of $(z-d)/L$ were $-0.03$ to $-8.5$ during dust devil observations during 12 and 13 July 2014 (Figure 8). In order to describe the atmospheric stability more clearly, we calculated the Richardson number between the surface and 10 m height every 10 min, based on the gradient detection system. The Richardson number ($Ri$) is named after Lewis Fry Richardson. Notably, $Ri$ has a single value corresponding with the value for $(z-d)/L$. It is the dimensionless number that expresses the ratio of the density gradient (the change in density with height) to the velocity gradient. The frequency distribution of atmospheric stability, using the stability classes A, B, C, D, E, and F, was subdivided by a Richardson criterion into strongly unstable, unstable, weakly unstable, neutral, weakly stable, and stable stratification, respectively (Table 2). Typically, a diurnal cycle of atmospheric stability shifted from nighttime stable to daytime unstable. Sixty-two percent of dust devils were observed in the atmospheric boundary layer with the weakly unstable stratification (class C), and none of dust devils happened during stable conditions (i.e., classes E and F).

### 3.3. Vertical Structure of a Dust Devil

We selected a typical dust devil with distance less than 100 m from the Xiaotang observation site, which lasted about 11 min around noon on 13 July 2014 to study the vertical structure of dust devils. In Figure 9,

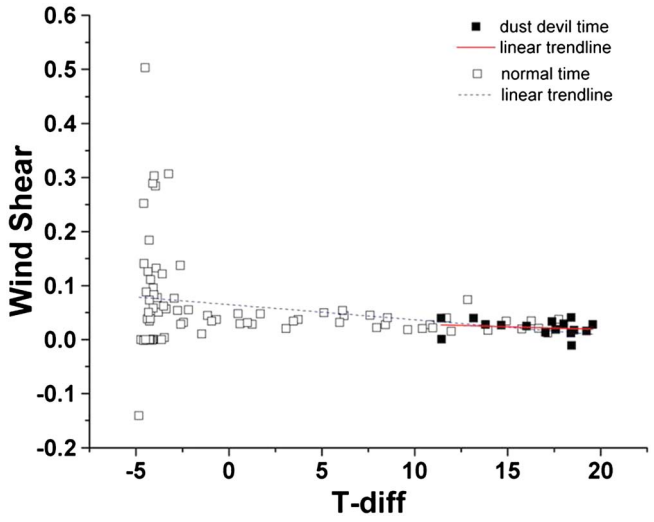


**Figure 7.** A scatter diagram of air-ground temperature difference (℃) and wind shear. Hollow and filled boxes represent the normal times and dust devil times, respectively. Solid and dashed lines represent different trend lines.

the circular arrows indicated the direction of anticlockwise rotation of the dust devil with the direction pointing to the north and south and moving direction of the dust devil from west to east. Three images present the beginning, mature, and end stages of the dust devil. At the beginning, the dust devil's diameter and height were relatively small at 12:29 P.M. In the mature stage, from 12:32 to 12:37 P.M., the dust devil reached a height of about 300 m with about 35 m in diameter. It was also observed in Australia that the height of dust devils was typically at least 5 times larger than its width [*Hess and Spillane*, 1990]. *Lorenz* [2013] proposed a relationship between lifetime ($t$) and diameter ($d$) with $t(d) = 40d^{0.66}$. In that study, the dust devil with a diameter of 35 m could last 400 s, which is two thirds the value of $t$ for our observed dust devil. There was about a 10% aspect ratio (height/diameter) that occurred more frequently than in Lorenz's study, which is consistent with the typical case of the dust devil over the TD. At the end stage of 12:39 P.M., the dust devil column cut off at the bottom and gradually vanished (Figure 9).

In this study, we focused on the variations of dust devil opacities near the surface to estimate the surface dust emission flux. Figure 10 displays the temporal changes of vertical opacity distributions at the northern, central, and southern parts in the lower dust devil column below 10 m. The opacity is calculated by averages of 30 pixels at the northern and southern edges as well as the center of dust devil column. During the process of the dust devil (Figure 10), the opacities at the northern part of the dust devil first exceeded 0.7 at 12:29 P.M.; the dust devil then developed with the high opacities of more than 0.9 at the northern and central parts at 12:33 P.M. The dust devil started to wane at 12:35 P.M. In the breakdown process, the dust opacities declined first at the center part of dust devil column and then the dust opacities dropped mostly below 0.3 in the lower dust devil column. Generally, the high dust particle concentrations correspond to larger dust opacities. When the center part of dust devil broke down, the dust devil could not bring the dust particles to the atmosphere anymore and then the northern and southern parts of dust devil began to gradually weaken.

It is pointed out that the high values of dust opacity did not appear near the ground all the time. At the northern part at 12:33 P.M. and the southern part of dust devil at 12:32 P.M., for instance, the peak opacities existed

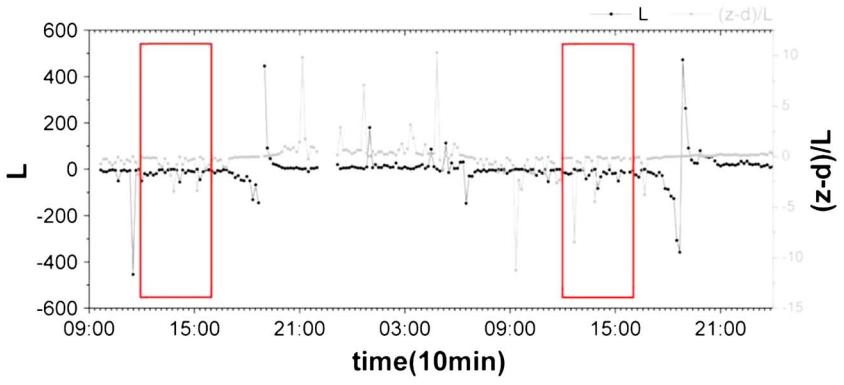


**Figure 8.** The 10 min changes in the Monin-Obukhov length $L$ (m) (black line) and the dimensionless stability factor $(z-d)/L$ (gray line) during 12 and 13 July 2014. Red boxes indicate when dust devils were observed.

**Table 2.** The Frequency of the Atmospheric Stability in 2 Days of 12 and 13 July 2014 and During the Period of Dust Devils[a]

| *Ri* | A(< −2.51) | B(−2.51 to −1.07) | C(−1.07 to −0.28) | D(−0.28–0.09) | E(0.09–0.13) | F(≥0.13) |
|---|---|---|---|---|---|---|
| 2 days | 6% | 9% | 23% | 26% | 8% | 27% |
| Dust devils | 12% | 15% | 62% | 11% | 0 | 0 |

[a]Classifying criteria of *Ri* with different atmospheric stability over plains.

at about 3 m, which could have resulted from the central updrafts and the peripheral downdrafts of dust particles in a rotating dust devil column (Figure 10), where the dust opacities were asymmetrically distributed with the northern high and southern low values (Figures 10a and 10c, respectively), reflecting an asymmetrical distribution of dust aerosol concentrations in the horizontal direction of dust devil column.

In the conventional situation, the solar signal is attenuated by absorption and scattering during the dust devil passage. In the study of *Lorenz and Jackson* [2015], two prominent dips in the solar signal may correspond to the wall of the dust devil (akin to the cloud wall closest to the center of the hurricane). For our observed opacity distribution, the maximum of the opacity values occurred in the northern part of dust devil, where the wall of the dust devil may be located. The rotating dust devil moved in the ambient wind direction from west to east. The rotating dust devil and the ambient wind could interact with the convergences (divergences) between rotating and ambient winds at the northern (southern) edges of dust devil, forming the asymmetrical distribution of dust opacities and aerosol particle concentrations.

### 3.4. Estimation of Surface Dust Emission Flux

Natural dust-lifting processes include dust devils, convective plumes, and dust storms. Dust emissions from dust devils are an unsolved issue in current aerosol modeling. Dust devils and dust plumes could contribute about 3.4%–35% of the global dust emissions to the atmosphere [*Jemmett-Smith et al.*, 2015; *Koch and Renno*, 2005]. In this section, we attempt to use the measured opacities of dust devils to estimate the vertical dust emission flux of a typical dust devil.

Based on the background dust concentrations and the dust size distribution estimated by the Pathfinder on the Mars [*Ferri et al.*, 2003; *Metzger*, 1999; *Tomasko et al.*, 1999], and the analysis of 348 dust devils and their opacities, *Greeley et al.* [2006] derived the approximate dust content $\delta$ in the unit of kg m$^{-2}$ from dust aerosol opacity

$$\delta = a\tau_d, \tag{5}$$

where $\tau_d$ is the opacity of dust devil and the factor of proportionality $a = 1.4 \times 10^{-3}$ kg m$^{-2}$ is given by *Greeley et al.*, 2006. The dust on the surface of the TD is assumed to have similar dust particle size distribution to that

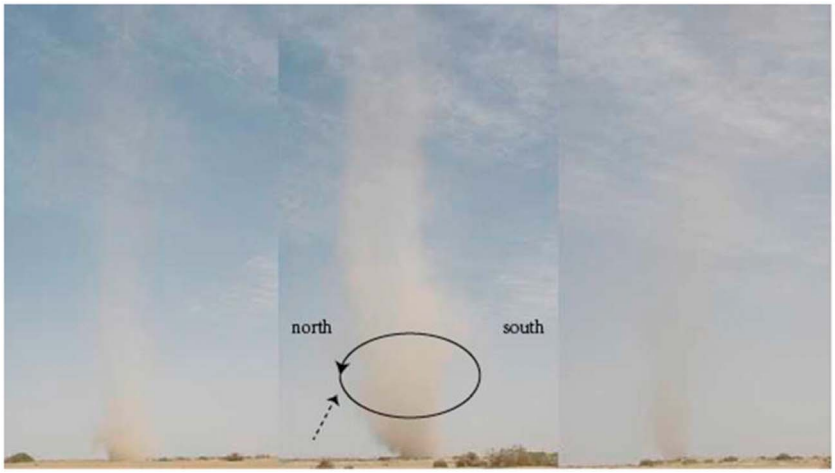


**Figure 9.** Three imagines of a dust devil event in the stages of (left) beginning at 12:30 P.M., (middle) mature at 12:33 P.M., and (right) end at 12:39 P.M. on 13 July 2014. The circular arrow shows the counterclockwise rotation of dust devil, and the dotted arrow shows the moving direction of dust devil from west to east.

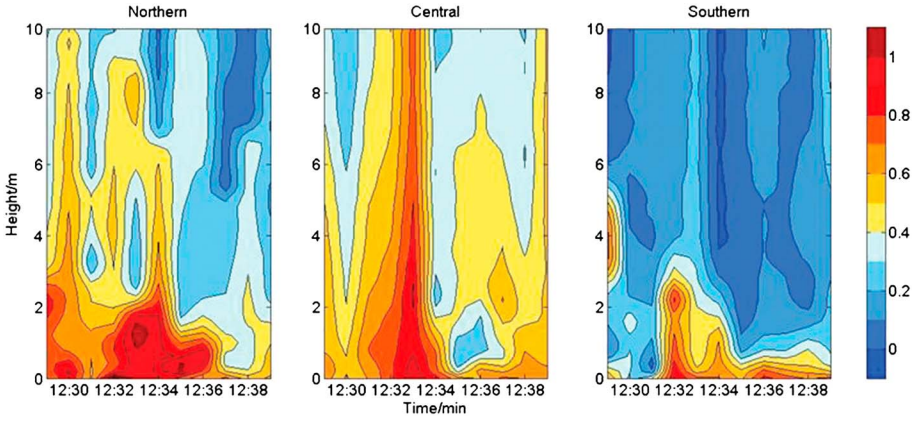


**Figure 10.** Temporal changes in the dust aerosol opacities of lower than 10 m at the northern, central, and southern parts of a dust devil observed from 12:29 to 12:39 P.M. on 13 July 2014.

of *Greeley et al*. [2006]; therefore, we adopted formula (4) to obtain the dust content for a dust devil over TD. Furthermore, the vertical dust emission flux $Q$ (kg m$^{-2}$ s$^{-1}$) is described by

$$Q = u\frac{\delta}{D} = u\frac{\tau_d}{D}\left(1.4\times10^{-3}\right), \tag{6}$$

where the vertical velocity $u$ was in the ambient air, observed at 2 m by the gradient detection system, in a range from 1.1 to 3.9 m s$^{-1}$ with a mean of 2.7 m s$^{-1}$ during the dust devil, and $D$ is the diameter of dust devil.

It should be indicated that$\tau$is the opacity of dust devil calculated from TD's dust devil observation in this study, while the $\tau_d$ used by *Greeley et al*. [2006] was the optical depth of a dust devil and was also referred to as the opacity of the dust raised by the dust devil. Opacity ($\tau$) of equation (1) corresponds to $1-\exp(-\tau_d)$ of equations (5) and (6). Under first approximation, this study adopted equations (5) and (6) from the study of *Greeley et al*. [2006] with the observed opacity ($\tau$) of equation (1) to roughly estimate the vertical dust emission flux of dust devils.

Table 3 gives the average diameters and opacities measured from the images of dust devil under 2 m, as well as the dust contents and vertical dust emission fluxes calculated with formulas (4) and (5). Because the height of the dust devil can hardly be distinguished with the cloud bottom, we did not show the height in the table. The dust aerosol opacities varied between 0.39 and 0.84 with the mean values of 0.56 during the dust devil process. Based on formula (4) in our study, the dust contents were estimated between 552 and 1180 mg m$^{-3}$, 1–3 times higher than the total suspended particle (TSP) concentration in a previous study [*Metzger et al*., 2011]. In the study of *Metzger et al*. [2011], the in situ (mobile) sampling of 33 natural dust devil vortices reveals a very high TSP mean value of 296 mg m$^{-3}$ and fine dust loading ($PM_{10}$) mean values ranging from 15.1 to 43.8 mg m$^{-3}$.

**Table 3.** The Average Diameters, the Opacities, the Calculated Dust Content, and Vertical Dust Emission Flux Under 2 m

| Time | Dust Devil Diameter (m) | Plume Opacity (–) | Dust Content (kg m$^{-2}$) | Dust Flux (kg m$^{-2}$ s$^{-1}$) |
|---|---|---|---|---|
| 12:29 | 25 | 0.58 | 8.09E−04 | 8.75E−05 |
| 12:30 | 32 | 0.48 | 6.79E−04 | 5.73E−05 |
| 12:31 | 31 | 0.52 | 7.23E−04 | 6.34E−05 |
| 12:32 | 33 | 0.74 | 1.04E−03 | 8.48E−05 |
| 12:33 | 33 | 0.84 | 1.18E−03 | 9.56E−05 |
| 12:34 | 31 | 0.72 | 1.13E−03 | 9.70E−05 |
| 12:35 | 29 | 0.48 | 6.40E−04 | 5.88E−05 |
| 12:36 | 31 | 0.49 | 6.87E−04 | 6.01E−05 |
| 12:37 | 34 | 0.48 | 6.71E−04 | 5.36E−05 |
| 12:38 | 25 | 0.42 | 5.83E−04 | 6.34E−05 |
| 12:39 | 26 | 0.39 | 5.52E−04 | 5.64E−05 |
| Average | 30 | 0.56 | 7.90E−04 | 7.07E−05 |

By using formula (5) and the measured near-surface wind speed, the vertical fluxes of near-surface dust emissions were estimated between $5.4\times10^{-5}$ and $9.6\times10^{-5}\,kg\,m^{-2}\,s^{-1}$ with the averages of $7.1\times10^{-5}\,kg\,m^{-2}\,s^{-1}$ during the dust devil observation. *Metzger et al.* [2011] obtained the mean dust emission fluxes of $0.9–7.5\times10^{-6}\,kg\,m^{-2}\,s^{-1}$, with the maximum from $4.3\,kg\,m^{-2}\,s^{-1}$ to $5.7\times10^{-5}\,kg\,m^{-2}\,s^{-1}$. *Gillette and Sinclair* [1990] estimated that a typical dust flux for dust devils in the southwestern America was about $2.8\times10^{-5}\,kg\,m^{-2}\,s^{-1}$. Our dust flux results are consistent with this previous study. Based on the observation on Mars, *Ferri et al.* [2003] estimated the vertical dust emission flux of $7\times10^{-5}\,kg\,m^{-2}\,s^{-1}$ for the dust devils by using a vertical wind speed of $20\,m\,s^{-1}$ and the dust aerosol loading values of *Metzger et al.* [1999]. The upward dust emission flux of a dust devil, recorded by the Spirit rover on Mars, was estimated from $4.0\times10^{-9}$ to $4.6\times10^{-4}\,kg\,m^{-2}\,s^{-1}$, with a mean value of $2.1\times10^{-5}\,kg\,m^{-2}\,s^{-1}$ [*Greeley et al.*, 2006]. The vertical fluxes of surface dust emissions in this study could be in a reasonable range for a dust devil event over TD in northwest China.

## 4. Conclusions

This study, based on a field observation of dust devils and atmospheric boundary layer from 7 to 14 July 2014, applied the digital optical method (DOM) to calculate dust opacity values of dust devils over the Taklimakan Desert (TD). A typical case of 13 July 2014 was selected with comprehensive images of the dust devil to analyze the formation mechanism, vertical structure, and dust emission of dust devils.

Dust devils tended to occur when the surface temperature differences between land and air were larger than 15°C. The extreme values of momentum flux and heat flux for dust devils could reach up to $0.54\,kg\,m^{-1}\,s^{-2}$ and $327\,W\,m^{-2}$, respectively. In addition, low wind shear with a wind shear index of less than 0.10 is necessary for dust devil formation. The unstable stratifications with well-developed convective boundary layer could be the sufficient condition for the formation of dust devils.

The maximum opacities for the central part of dust devil were observed on the ground. However, the peak opacity values in the peripheral parts of the dust devil existed at a height of about 3 m in the dust devil's column. The dust devil had an asymmetrical distribution of dust aerosol concentrations and opacities in the horizontal section, as a result of the interaction of the tangential velocity of rotating dust devils and the ambient wind. In a typical evolution of a dust devil over TD, the vertical fluxes of near-surface dust emissions were estimated in a range from $5.4\times10^{-5}$ to $9.6\times10^{-5}\,kg\,m^{-2}\,s^{-1}$.

Based on the available observations of surface heating and atmospheric boundary layer conditions, the critical conditions in the atmospheric boundary layer for dust devil formation were identified with a field observation over the Taklimakan Desert by investigating the thermal and dynamical conditions in understanding of formation mechanism of dust devils. Unfortunately, funding is not available to provide more thorough statistics about the plumes detected during the field campaign. The detailed and integrated mechanism for the dust devil will be revealed from the further comprehensive field measurements. In the further study, the internal structures of dust devils, including air temperature and pressure as well as dust size distribution, should be measured in the long-term observation to better understand the dust devils' formation mechanism. This work is useful in the parameterization of dust emission for future modeling of the impact of dust devils on the atmospheric environment and climate change.

**Acknowledgments**
This research was supported by the National Natural Science Foundation of China (41175093, 41375158, 41405013, and 41375163) and the Research Starting Project of NUIST (20110304) of China.
The corresponding author is Tianliang Zhao (e-mail: tlzhao@nuist.edu.cn) at Nanjing University of Information Science and Technology, Nanjing 210044, China.

## References

Balme, M., and R. Greeley (2006), Dust devils on Earth and Mars, *Rev. Geophys.*, *44*, RG3003, doi:10.1029/2005RG000188.
Carroll, J. J., and J. A. Ryan (1970), Atmospheric vorticity and dust devil rotation, *J. Geophys. Res.*, *75*(27), 5179–5184.
Du, K. (2007), Optical remote sensing of airborne particulate matter to quantify opacity and mass emissions, Civil and Environ. Eng., Univ. of Illinois at Urbana-Champaign, Urbana, 145 pp.
Du, K., M. J. Rood, B. J. Kim, M. R. Kemme, B. Franek, and K. Mattison (2007), Quantification of plume opacity by digital photography, *Environ. Sci. Technol.*, *41*(3), 928–935.
Du, K., P. Shi, M. J. Rood, K. Wang, Y. Wang, and R. M. Varma (2013), Digital optical method to quantify the visual opacity of fugitive plumes, *Atmos. Environ.*, *77*, 983–989, doi:10.1016/j.atmosenv.2013.06.017.
Farrugia, R. (2003), The wind shear exponent in a Mediterranean island climate, *Renew. Energy*, *28*(4), 647–653.
Ferri, F., P. H. Smith, M. Lemmon, and N. O. Rennó (2003), Dust devils as observed by Mars Pathfinder, *J. Geophys. Res.*, *108*(E12), 5133, doi:10.1029/2000JE001421.
Gillette, D. A., and P. C. Sinclair (1990), Estimation of suspension of alkaline material by dust devils in the United States, *Atmos. Environ., Part A*, *24*(5), 1135–1142.

Greeley, R., et al. (2006), Active dust devils in Gusev crater, Mars: Observations from the Mars Exploration Rover Spirit, *J. Geophys. Res.*, *111*, E12S09, doi:10.1029/2006JE002743.
Gu, Z., Y. Zhao, and Y. Yu (2003), Numerical study of the formation evolution and structure of dust devil, *Acta Metall. Sin. (Chin.)*, *61*(6), 751–760.
Hallett, J., and T. Hoffer (1971), Dust devil systems, *Weather*, *26*(6), 247–250.
Han, C., A. Q. Huang, M. E. Baran, and S. Bhattacharya (2008), STATCOM impact study on the integration of a large wind farm into a weak loop power system, *Power Systems Conference and Exposition*, *Psce 06*, *IEEE Pes*, *23* (1), 226 - 233.
Hess, G., and K. Spillane (1990), Characteristics of dust devils in Australia, *J. Appl. Meteorol.*, *29*(6), 498–507.
Hess, G., K. Spillane, and R. Lourensz (1988), Atmospheric vortices in shallow convection, *J. Appl. Meteorol.*, *27*(3), 305–317.
Ives, R. L. (1947), Behavior of dust devils, *Bull. Am. Meteorol. Soc.*, *28*, 168–174.
Jemmett-Smith, B. C., J. H. Marsham, P. Knippertz, and C. A. Gilkeson (2015), Quantifying global dust devil occurrence from meteorological analyses, *Geophys. Res. Lett.*, *42*, 1275–1282, doi:10.1002/2015GL063078.
Kim, B., M. Rood, and K. Du (2007), Scientific and technical basis for the innovative digital optical method (DOM) to ,measure plume opacity using digital camera images, Tech. Rep., U.S. Army Engineer Research and Development Center - Construction Engineering Research Laboratory (ERDC-CERL), Champaign, Ill.
Koch, J., and N. O. Renno (2005), The role of convective plumes and vortices on the global aerosol budget, *Geophys. Res. Lett.*, *32*, L18806, doi:10.1029/2005GL023420.
Lorenz, R. D. (2013), The longevity and aspect ratio of dust devils: Effects on detection efficiencies and comparison of landed and orbital imaging at mars, *Icarus*, *226*(1), 964–970.
Lorenz, R. D., and B. K. Jackson (2015), Dust devils and dustless vortices on a desert playa observed with surface pressure and solar flux logging, *GeoResJ*, *5*, 1–11, doi:10.1016/j.grj.2014.11.002.
Lorenz, R. D., and M. J. Myers (2005), Dust devil hazard to aviation: A review of United States air accident reports, *J. Meteorol.*, *30*(298), 178–184.
Lorenz, R. D., B. Jackson, and J. Barnes (2010), Inexpensive time-lapse digital cameras for studying transient meteorological phenomena: Dust devils and playa flooding, *J. Atmos. Oceanic Technol.*, *27*, 246–256.
Lyons, T. J., U. S. Nair, and I. J. Foster (2008), Clearing enhances dust devil formation, *J. Arid Environ.*, *72*(10), 1918–1928, doi:10.1016/j.jaridenv.2008.05.009.
Malin, M. C., and K. S. Edgett (2001), Mars Global Surveyor Mars Orbiter Camera: Interplanetary cruise through primary mission, *J. Geophys. Res.*, *106*(E10), 23,429–23,570.
Mamtimin, A., H. Qing, G. Zhi-qiu, A. Sayit, H. Wen, L. Xin-chun, and L. Yun (2008), Comparison of calculation methods for turbulent heat flux over atmosphere surface layer in Taklimakan Desert, *J. Desert Res.*, *28*(5), 948–954.
Mattsson, J. O., T. Nihlén, and W. Yue (1993), Observations of dust devils in a semi-arid district of southern Tunisia, *Weather*, *48*(11), 359–363.
Metzger, S. M. (1999), Dust devils as aeolian transport mechanisms in southern Nevada and the Mars Pathfinder landing site, PhD thesis, Univ. of Nev., Reno.
Metzger, S. M., J. R. Carr, J. R. Johnson, T. J. Parker, and M. T. Lemmon (1999), Dust devil vortices seen by the Mars Pathfinder Camera, *Geophys. Res. Lett.*, *26*(18), 2781–2784, doi:10.1029/1999GL008341.
Metzger, S. M., M. R. Balme, M. C. Towner, B. J. Bos, T. J. Ringrose, and M. R. Patel (2011), In situ measurements of particle load and transport in dust devils, *Icarus*, *214*(2), 766–772.
Oke, A., N. Tapper, and D. Dunkerley (2007), Willy-willies in the Australian landscape: The role of key meteorological variables and surface conditions in defining frequency and spatial characteristics, *J. Arid Environ.*, *71*(2), 201–215.
Reiss, D., J. Raack, A. P. Rossi, G. D. Achille, and H. Hiesinger (2010), First in-situ analysis of dust devil tracks on Earth and their comparison with tracks on Mars, *Geophys. Res. Lett.*, *37*, L14203, doi:10.1029/2010GL044016.
Reiss, D., J. Raack, and H. Hiesinger (2011), Bright dust devil tracks on Earth: Implications for their formation on Mars, *Icarus*, *211*(1), 917–920.
Rennó, N. O., M. L. Burkett, and M. P. Larkin (1998), A simple thermodynamical theory for dust devils, *J. Atmos. Sci.*, *55*(21), 3244–3252.
Renno, N. O., V. J. Abreu, J. Koch, P. H. Smith, O. K. Hartogensis, H. A. De Bruin, D. Burose, G. T. Delory, W. M. Farrell, and C. J. Watts (2004), MATADOR 2002: A pilot field experiment on convective plumes and dust devils, *J. Geophys. Res.*, *109*, E07001, doi:10.1029/2003JE002219.
Roland, S. (2000), *Meteorology for Scientists and Engineers*, 502 pp., Brooks Cole, Pacific Grove, Calif.
Sinclair, P. C. (1964), Some preliminary dust devil measurements, *Mon. Weather Rev.*, *92*(8), 363–367.
Sinclair, P. C. (1973), The lower structure of dust devils, *J. Atmos. Sci.*, *30*(8), 1599–1619.
Snow, J. T., and T. M. McClelland (1990), Dust devils at white sands missile range, New Mexico: 1. Temporal and spatial distributions, *J. Geophys. Res.*, *95*(D9), 13,707–13,721.
Tomasko, M., L. Doose, M. Lemmon, P. Smith, and E. Wegryn (1999), Properties of dust in the Martian atmosphere from the Imager on Mars Pathfinder, *J. Geophys. Res.*, *104*(E4), 8987–9007.
Whelley, P. L., and R. Greeley (2008), The distribution of dust devil activity on Mars, *J. Geophys. Res.*, *113*, E07002, doi:10.1029/2007JE002966.
Zhang, R. J., Q. He, D. Kong, and F. Chen (2008), Study on grain size characteristics of surface sediment in sandstorm source regions in the Northern Marginal Zone of the Taklimakan Desert, *Arid Zone Res.*, *25*(6), 887–893.